JGR Oceans

RESEARCH ARTICLE
10.1029/2020JC016046

Key Points:
- High-resolution Southern Ocean simulations suggest that current-wind-stress interaction on the mesoscale reduces eddy kinetic energy by 25%
- Current-wind interaction induces a net upward linear but downward nonlinear modulation of Ekman pumping rates
- Current-wind interaction enhances stratification near the bottom of the mixed layer by up to 10%

Supporting Information:
- Supporting Information S1

Correspondence to:
H. Song,
hajsong@yonsei.ac.kr

Citation:
Song, H., Marshall, J., McGillicuddy, D. J., & Seo, H. (2020). Impact of current-wind interaction on vertical processes in the Southern Ocean. *Journal of Geophysical Research: Oceans*, *125*, e2020JC016046. https://doi.org/10.1029/2020JC016046

Received 3 JAN 2020
Accepted 14 MAR 2020
Accepted article online 17 MAR 2020

Impact of Current-Wind Interaction on Vertical Processes in the Southern Ocean

Hajoon Song[1], John Marshall[2], Dennis J. McGillicuddy Jr.[3], and Hyodae Seo[4]

[1]Department of Atmospheric Sciences, Yonsei University, Seoul, Republic of Korea, [2]Department of Earth, Atmospheric and Planetary Sciences, Massachusetts Institute of Technology, Cambridge, MA, USA, [3]Department of Applied Ocean Physics and Engineering, Woods Hole Oceanographic Institution, Woods Hole, MA, USA, [4]Physical Oceanography Department, Woods Hole Oceanographic Institution, Woods Hole, MA, USA

Abstract Momentum input from westerly winds blowing over the Southern Ocean can be modulated by mesoscale surface currents and result in changes in large-scale ocean circulation. Here, using an eddy-resolving 1/20 degree ocean model configured near Drake Passage, we evaluate the impact of current-wind interaction on vertical processes. We find a reduction in momentum input from the wind, reduced eddy kinetic energy, and a modification of Ekman pumping rates. Wind stress curl resulting from current-wind interaction leads to net upward motion, while the nonlinear Ekman pumping term associated with horizontal gradients of relative vorticity induces net downward motion. The spatially averaged mixed layer depth estimated using a density criteria is shoaled slightly by current-wind interaction. Current-wind interaction, on the other hand, enhances the stratification in the thermocline below the mixed layer. Such changes have the potential to alter biogeochemical processes including nutrient supply, biological productivity, and air-sea carbon dioxide exchange.

Plain Language Summary Momentum transfer between winds blowing over the Southern Ocean depends on the relative speed of the winds and surface currents. Mesoscale eddies with a scale of 100 km or less are very vigorous and thus can modulate momentum transfer. Here, we use an ocean model with sufficiently high horizontal resolution that it can resolve the mesoscale and hence capture the modulation. We find a reduction in the momentum transfer from the wind to the ocean and a reduction in eddy kinetic energy, together with a modification of wind-driven vertical motion. Structural changes in the wind stress field modify patterns of upwelling and downwelling in a manner that can be understood from nonlinear Ekman theory. Moreover, current-wind interaction results in an increase in the stratification below the mixed layer and hence a reduced communication between the surface and the interior ocean. There is thus a potential impact on biogeochemical processes and the climate of the Southern Ocean.

1. Introduction

Both satellite observations and atmospheric reanalyses show the world's strongest winds blow over the Southern Ocean (Tsujino et al., 2018). Underneath, and driven by the westerly winds, flows an ocean current directed generally eastward with speeds of several tens of cm s^{-1} (Dohan & Maximenko, 2010; Laurindo et al., 2017; Maximenko et al., 2009). This Antarctic circumpolar current (ACC) circumnavigates the globe passing through Drake Passage near 60°S (Talley et al., 2011). While both winds and currents generally flow eastward, the wind blows faster than the currents, and so there is a continuous transfer of momentum from the wind to the ocean. The stress $\tau = (\tau_x, \tau_y)$ at the surface is given by

$$\boldsymbol{\tau} = \rho_a C_D \left(\mathbf{u}_a - \mathbf{u}_o\right) |\mathbf{u}_a - \mathbf{u}_o|, \tag{1}$$

where $(\mathbf{u}_a = (u_{a,x}, u_{a,y}))$ is the 10-m wind, $(\mathbf{u}_o = (u_{o,x}, u_{o,y}))$ is the surface current, and ρ_a, C_D are the air density and drag coefficient, respectively (Large & Yeager, 2004). The 10-m wind is the main source of wind stress variability because winds have shorter timescales than ocean currents, especially in the storms blowing over the ACC. Often the effect of ocean currents on the surface stress is neglected because $|\mathbf{u}_a| \gg |\mathbf{u}_o|$. However, in turbulent oceanic regimes such as the Southern Ocean, where the spatial scale of the surface currents is much shorter than that of the wind, this assumption must be reevaluated: The wind stress and its curl can be significantly affected by the presence of the ocean's mesoscale.

The prevailing westerly wind leads to equatorward Ekman transport and upwelling to the south of the ACC. As a result, isopycnals shoal and the ocean gain available potential energy. This is then converted to eddy kinetic energy via baroclinic instability resulting in the ubiquitous meanders and mesoscale eddies typical of the ACC. These mesoscale features constantly change the direction of the flow, leaving imprints on the wind stress field through equation(1), such that the wind stress increases/decreases when the ocean flows in the opposite/same direction of the wind. This occurs on spatial scales characterized by the oceanic first baroclinic Rossby radius of deformation which is generally less than 30 km along the ACC (Chelton et al., 1998; Tulloch et al., 2011). In the special case of mesoscale eddies possessing vorticity over which a uniform wind without vorticity blows, one "side" of the ocean eddy has enhanced stress relative to the other. This "top drag" effect (Dewar & Flierl, 1987) dampens mesoscale eddies (Duhaut & Straub, 2006; Dawe & Thompson, 2006; Eden & Dietze, 2009; Zhai et al., 2012). This current-wind interaction, also known as the effect of "relative wind stress," is believed to dampen mesoscale eddies in many parts of the world's oceans. For example, in modeling and observational studies, the eddy kinetic energy (EKE) can be decreased by 10% in the northwest Atlantic Ocean (Zhai & Greatbatch, 2007), 25% in the Arabian Sea (Seo, 2017) and the Agulhas Current (Renault, McWilliams, & Penven, 2017), 30% in the Gulf Stream (Renault et al., 2016), approximately 50% in the California Current System (Renault et al., 2016; Seo et al., 2016), and even by as much as 100% in the Bay of Bengal (Seo et al., 2019).

The Southern Ocean is not exceptional in respect to the reduction of EKE through eddy-wind interaction. Hutchinson et al. (2010) report the reduction of kinetic energy in the standing and transient eddies by 11% and 18%, respectively, in their eddy-resolving quasi-geostrophic model driven by a zonally symmetric westerly wind. The reduction of the surface EKE by current-wind interaction is approximately 15% in the idealized channel model experiments reported by Munday and Zhai (2015). They further show that the degree of reduction is sensitive to the total power input by the wind. Current-wind interaction also increases the transport of the ACC and results in steeper isopycnals (Munday & Zhai, 2015). Moreover, satellite observations show that the impact of ocean currents on wind stress is the greatest in the Southern Ocean (Renault, McWilliams, & Masson, 2017).

Although such studies advance our understanding of the impact of ocean current on momentum flux in the Southern Ocean, there are many unanswered questions. First, what is the effect of current-wind interaction on vertical motion? In particular, the Southern Ocean is rich in meanders and eddies, where both linear and nonlinear Ekman pumping contributions are likely to be important. Second, can current-wind interaction affect vertical mixing and the stratification of the upper ocean? When wind energy input is reduced by including relative wind stress, one may anticipate a weakening of vertical mixing. However, this effect might be reinforced or offset by changes in stratification in the upper ocean resulting from changes in wind-driven Ekman pumping. Can we parse these effects to arrive at an understanding of the net effect? Furthermore, given that upper ocean stratification and the mixed layer depth (MLD) exhibit large seasonality (de Boyer Montégut et al., 2004; Dong et al., 2008; Holte & Talley, 2009; Hausmann et al., 2017), we should necessarily focus on the seasonality of the response, which has been absent in previous studies.

In this study, we utilize a high-resolution ocean model in a realistic configuration and investigate current-wind interaction near Drake Passage. Our analysis method is straightforward. We compare two simulations, one with and one without current-wind interaction to quantify the effects. Consistent with previous studies, we document a reduction in EKE when the full interaction is included, such that it approaches levels observed from satellite data. The net change of the total Ekman pumping is not significant, but both linear and nonlinear contributions show compensating modifications. Although the mean mixed layer depth is not altered, we observe an increase in the stratification of the upper thermocline, especially in austral summer.

Our study is set out as follows. Section 2 contains a detailed description of the experimental design. The model results are evaluated by computing changes in the wind stress and EKE in section 3. We then analyze changes in the vertical velocity, vertical mixing, and stratification in section 4. We conclude in section 5 with a discussion of the results.

2. Experimental Design

The effect of current-wind interaction is investigated using the Massachusetts Institute of Technology general circulation model (MITgcm) (Adcroft et al., 1997, 2004; Marshall, Hill et al., 1997; Marshall, Adcroft et al., 1997; Marshall et al., 1998). The study area includes the Drake Passage and its upstream/downstream

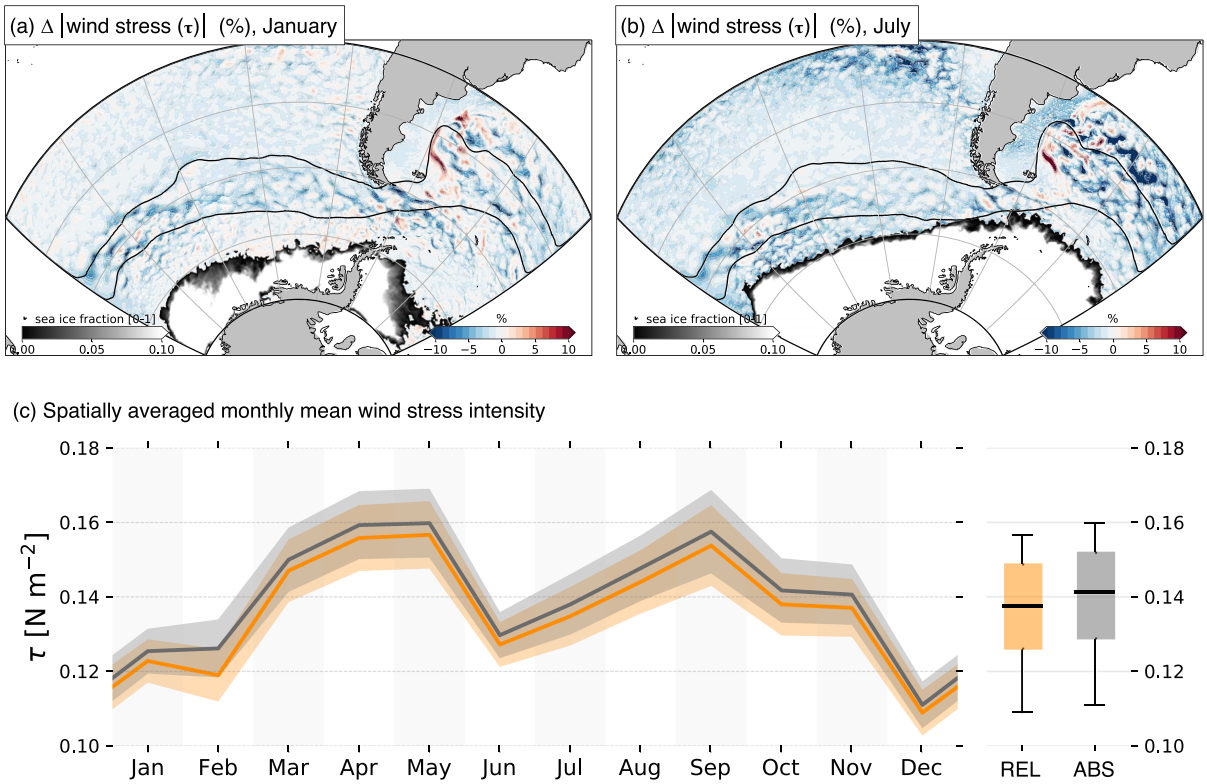

Figure 1. Monthly averaged wind stress intensity changes ($\Delta|\tau| = 100 \times (|\tau_{REL}| - |\tau_{ABS}|)/|\tau_{ABS}|$) in (a) January and (b) July. Black solid lines indicate the approximate bound of the ACC based on the sea level height. The same bound is applied for both REL and ABS. Sea ice fractions are shown in gray scale. Time series of the monthly averaged wind stress intensity along the ACC (marked by black solid lines in panels a and b) in REL and ABS are shown in orange and gray, respectively, in (c). The shading in (c) represents the 95% confidence interval. In the box plot in (c), the whiskers represent the range of the data, while the height of the box and the black line are the range of the lower to upper quartile and median value, respectively.

regions in the Southern Ocean, covering a 140° longitudinal swath. The ACC snakes through the domain that ranges from 75°S to 35°S (Figure 1a). The horizontal resolution is 0.05° or roughly 4 km along the ACC, enabling us to resolve the mesoscale. The model was integrated for 5 years driven by the surface atmospheric fields from the Interim European Centre for Medium-Range Weather Forecasts (ECMWF) Re-Analysis 6-hourly data (Simmons et al., 2007) and monthly mean lateral boundary condition taken from the Ocean Comprehensive Atlas, a data assimilated product (Forget, 2010). During the simulation, surface heat and freshwater fluxes are computed from bulk formulae (Large & Yeager, 2004), and the 10-m wind, neglecting current-wind interaction. Vertical mixing is calculated using the K-profile parameterization (KPP) scheme of Large et al. (1994). KPP first estimates the mixing depth, h, using a Richardson number criterion determined from the surface forcing, the vertical buoyancy gradient, and the current shear. The eddy diffusivity is then computed using h, a turbulent velocity scale, and a vertical shape function. This simulation is referred to as ABS as it uses the absolute wind stress.

This configuration has its root in the simulation of Tulloch et al. (2014) which was thoroughly compared with observations. The 100 vertical levels of the Tulloch configuration were reduced to 50 in which the top 100 m is represented at 10-m resolution. Despite reduced vertical resolution, the 50-level configuration remains qualitatively similar to observations such as EKE and MLD. This configuration has also been successfully coupled with a biogeochemical model for both online (Song et al., 2015, 2016) and offline simulations (Song et al., 2019).

The effect of current-wind interaction is explored by comparing ABS with a simulation in which the wind relative to the surface ocean current is used in the wind stress calculation as in (1). This simulation, referred to as REL, otherwise has the same configuration as ABS, and so differences between ABS and REL can be attributed to the current-wind interaction. It is noted that this model is not coupled to an atmospheric model so that the sea surface temperature (SST) anomaly does not affect the stability of the atmospheric

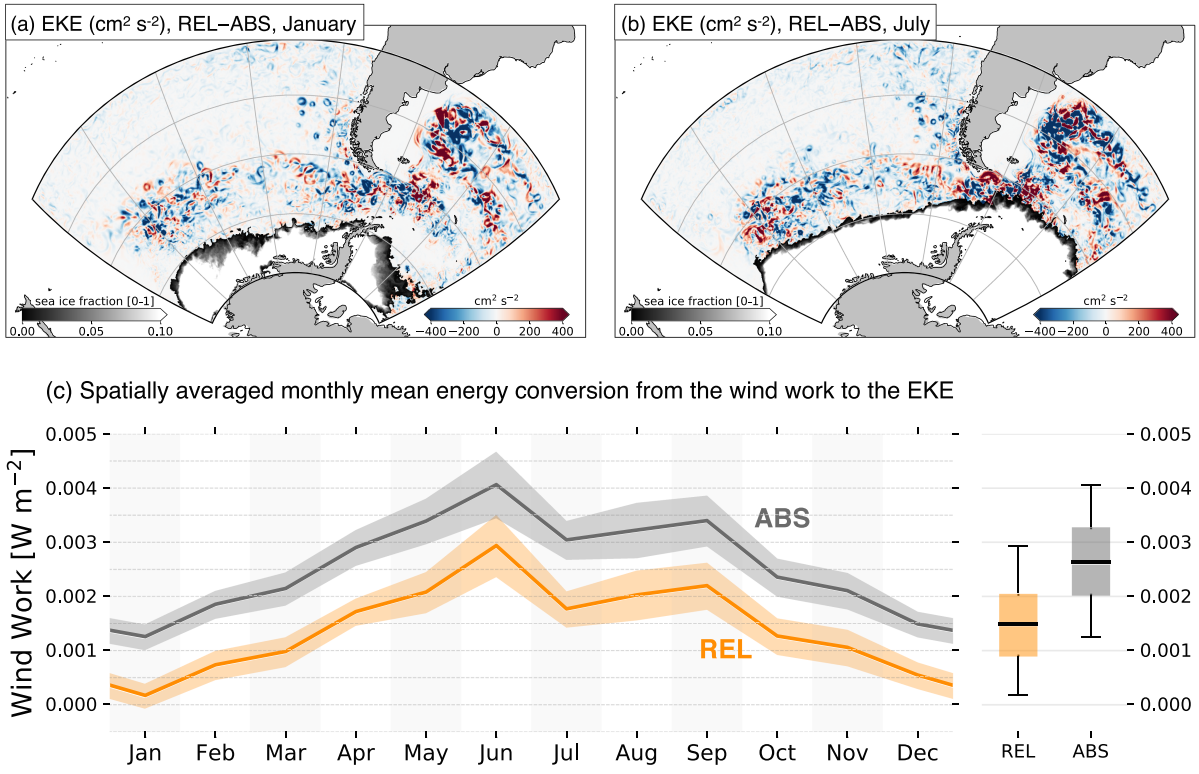

Figure 2. The difference in the monthly mean surface eddy kinetic energy (EKE, $0.5\,\overline{(u'^2+v'^2)}$) computed using 5-day mean velocities in (a) January and (b) July. The sea ice fractions in the model simulation are plotted in the gray scale. In (c), the monthly mean values of the energy conversion from the wind work to the EKE along the ACC (marked by black solid lines in Figure 1) in the ABS and REL simulations are plotted. The description of the bar plots is in Figure 1.

boundary layer and 10-m wind, which potentially alter the results. Also the responses of the different wind stress estimation can be underestimated because the atmospheric condition is prescribed and restores SST according to it.

Simulating ABS and REL at high resolution is demanding of computing power, and so we only integrate REL for three and a half years. In REL, EKE is rapidly reduced for the first 3 months, followed by a modest decrease of EKE during the rest of the integration (not shown). Although the simulations do not necessarily achieve a statistically steady state over the 3.5-year period, it is sufficient for us to analyze the effect of current-wind interactions since the magnitude of the difference in EKE between REL and ABS does not continue to increase beyond the first few months of simulation. The first 6 months were regarded as the spin-up period, and the last 3 years of simulation were the focus of our analysis.

3. The Impact of Current-Wind Interaction on Upper Ocean Energy

3.1. Wind Stress Changes

The reduction of wind stress can be anticipated in the Southern Ocean where the westerly wind blows over the eastward current. Indeed, the wind stress is reduced in most of the model domain except in limited areas where the current flows in the opposite direction of the wind (Figures 1a and 1b). The average reduction is not large (less than 3%) in both austral summer and winter, although there are regions where the reduction can be as large as 10% near to the axis of the ACC. The reduction in the wind stress persists all year round along the ACC, with little sign of a seasonal cycle (Figure 1c). This result is consistent with previous studies (Hutchinson et al., 2010; Munday & Zhai, 2015) where the reduction of the wind stress is in the range of 2% to 10%.

The reduced eastward wind stress in REL decreases the wind-driven Ekman transport toward the equator. The influence of this change on the mean circulation in REL can be muted when it is constrained by the same boundary conditions as ABS (supporting information Figure S1). Since the same boundary conditions are applied to both ABS and REL, instead of using zonal transport, we analyze the impact of the

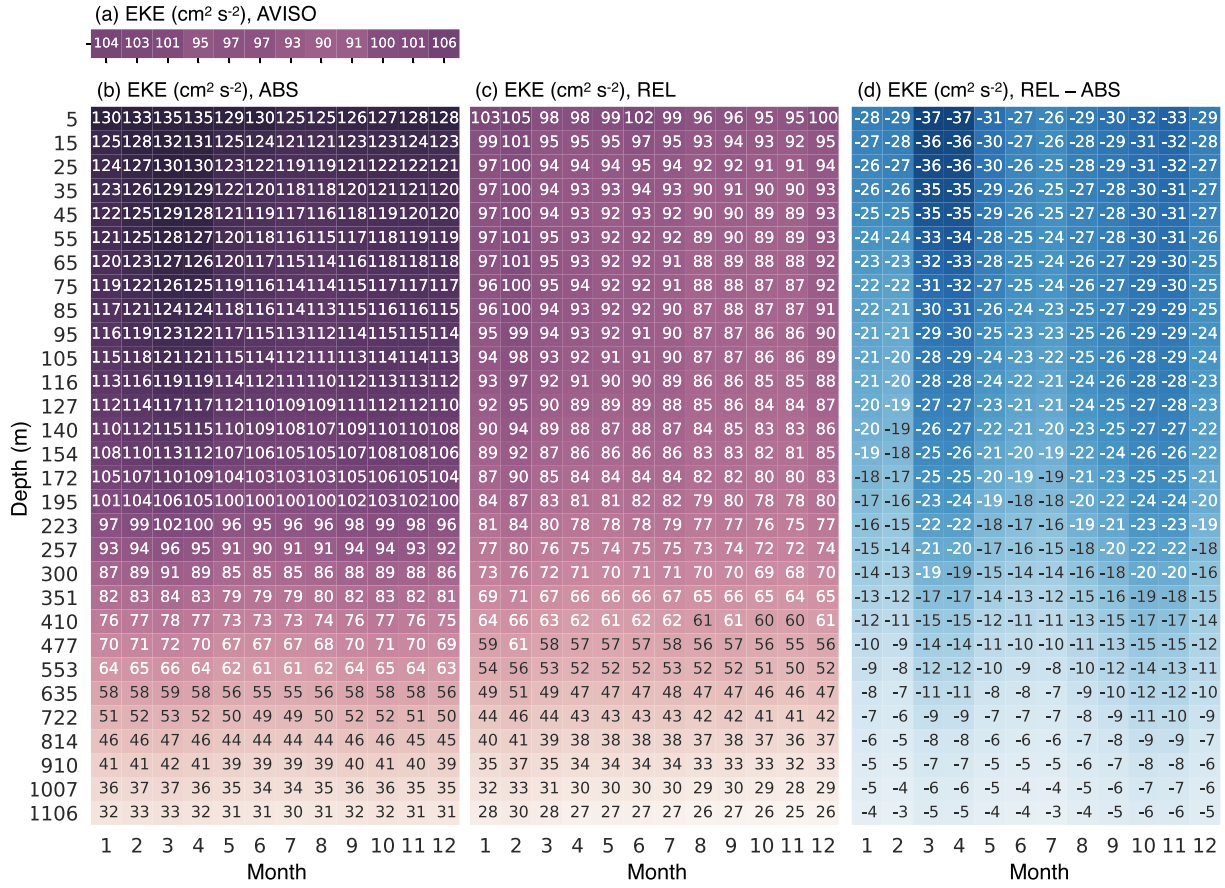

Figure 3. (a) The monthly mean EKE at the surface averaged over the model domain calculated using AVISO product. The monthly mean EKE values as a function of month and depth in ABS and REL are shown in (b) and (c), respectively. Panel (d) is the difference in the monthly mean EKE between ABS and REL.

weaker Ekman transport on the conversion of the mean potential energy to mean kinetic energy by computing $-g/\rho_0 \int \langle\rho\rangle\langle w\rangle dz$. Although the change is only $O(0.1°)$, the latitudes where isopycnals outcrop in REL are further south than in ABS between 65°S and 45°S (Figure 8). This is consistent with Ekman transport being weaker in REL. The conversion from mean potential energy to mean kinetic energy is less in REL by approximately 3% in the top 350 m over this latitude band. Despite the small differences, reduced energy conversion suggests that there is a lower level of potential energy available for conversion to kinetic energy, as expected because of the weaker Ekman transport in REL.

3.2. Eddy Kinetic Energy Changes

The ACC and Brazil–Malvinas Confluence Zone are known for their high level of the EKE (Wunsch, 2007), and this spatial pattern of EKE is well represented in ABS and REL with no clear seasonal variability (not shown). The different maps of the EKE between ABS and REL show positive and negative values occurring in proximity along the ACC (Figures 2a and 2b), probably the result of lateral shifts in mesoscale features. However, EKE is generally lower in REL than in ABL, particularly to the north of the ACC.

Indeed, the spatially averaged EKE is always lower in REL than in ABS, not only at the surface but also over the top 1,000 m at all times (Figure 3). On average, the current-wind interaction reduces the surface EKE by approximately 24%, which is slightly greater than the reduction reported in the Southern Ocean in other studies (Hutchinson et al., 2010; Munday & Zhai, 2015). Although the maximum reduction of the surface EKE occurs in April (up to 28%), there is no clear seasonality in the signal. The current-wind interaction alleviates overestimation of EKE in ABS, and the spatially averaged EKE values in REL compare much better with those obtained using geostrophic current derived from the Ssalto/Duacs gridded sea level anomaly data (Figures 3a–3c).

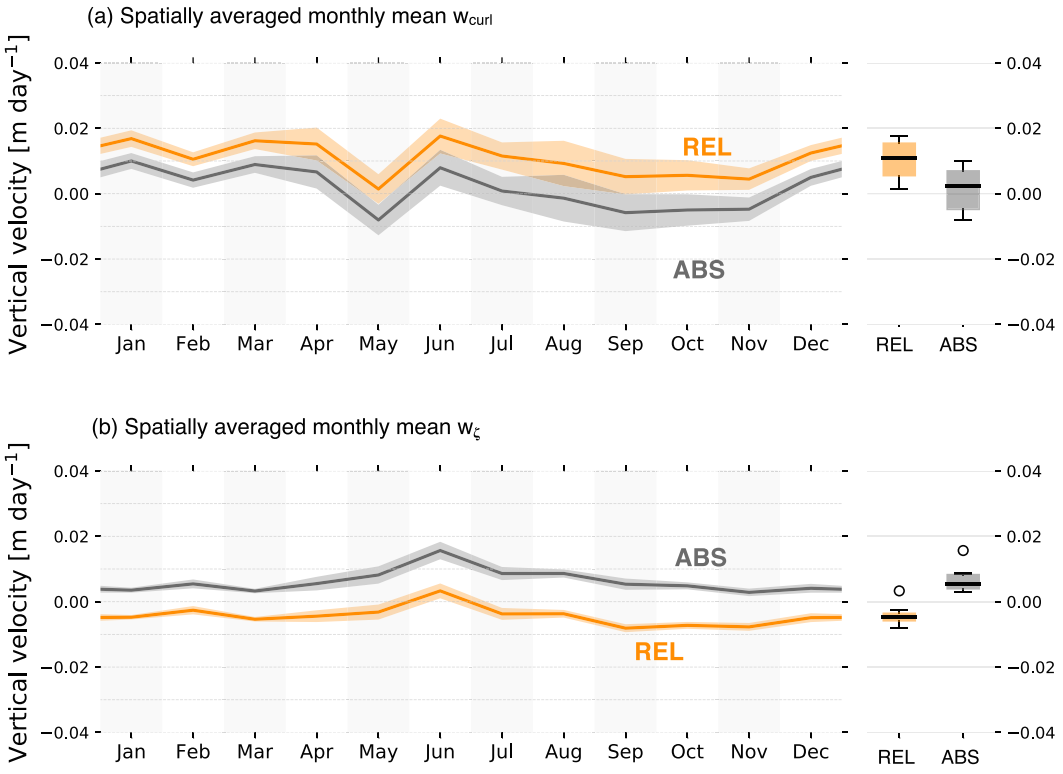

Figure 4. The monthly mean values of (a) wind-driven vertical velocity by wind stress curl (w_{curl}) and (b) lateral gradient of vorticity (w_{ζ}) along the ACC (marked by black solid lines in Figure 1) in the ABS and REL simulations. The description of the bar plots is in Figure 1.

A nonlinear least-squares fit shows that the vertical profile of EKE in ABS decays exponentially with depth with a scale of ~775 m. In REL, the EKE vertical profile also follows an exponential function but with a decay scale of ~850 m, indicating that the EKE in REL decreases less rapidly than in ABS with depth, reflecting the more pronounced surface decrease in EKE in REL. Even though the magnitude of the reduction at depth is much smaller than those at the surface, the percentage reduction of the mean EKE reduction is still reasonably large; at 1,106 m the EKE in REL is approximately 14% less than that in ABS.

The reduction of EKE in REL suggests that the energy conversion from its sources is decreased. Three major conversion processes are wind work, barotropic instability, and baroclinic instability (Marchesiello et al., 2003; Seo et al., 2016; Zhan et al., 2016). We find that the reduction in EKE in REL originates primarily from reduced levels of wind work $\left(\overline{u'\tau'_x} + \overline{v'\tau'_y}\right)$ (Figure 2c). There are smaller differences in barotropic and baroclinic contributions to the EKE (Figure S2), consistent with previous studies (i.e., Seo et al., 2016). Changes in energy input from the wind are identified as the main cause of reduced EKE in previous studies (Oerder et al., 2018; Seo et al., 2016), suggesting a robustness in the impact of current-wind interaction on the energetic analysis. Reduction of the wind work is similar in each month (Figure 2c). The annual mean reduction of the wind work is more than 40%, which is greater than that reported in the earlier work in the Southern Ocean (Hutchinson et al., 2010).

4. Impact on Vertical Processes

4.1. Wind-Driven Vertical Velocity

The current-wind interaction alters not only the wind stress but also its curl, and so we anticipate modifications to the Ekman Pumping rates, w_{curl}. When relative vorticity is not negligible, as in our simulation where the Rossby number (Ro) $O(0.1)$, there is a nonlinear contribution (w_{ζ}) to the Ekman pumping velocity (McGillicuddy et al., 2008; Niiler, 1969; Stern, 1965; Wenegrat & Thomas, 2017). In this case the Ekman pumping velocity (w_{tot}) is given by

$$w_{tot} \approx w_{curl} + w_{\zeta} \tag{2}$$

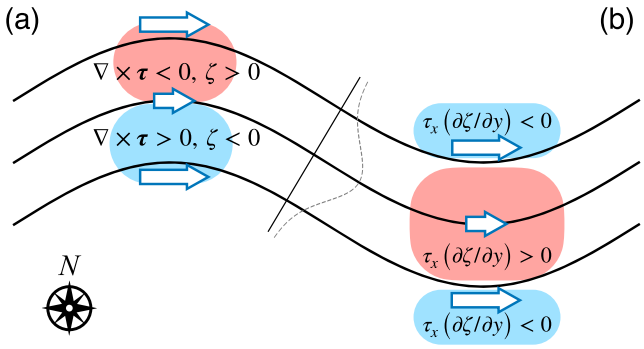

Figure 5. A diagram that visualizes the wind-driven vertical velocity estimated by (3–4) along an idealized meander enveloped by two outer black solid lines under a uniform zonal wind. The black solid line at the center represents the core axis of the meander as the current speed is shown by dashed line. The interaction between the current and wind reduces τ_x (white arrows) along the main axis of the meander. Red and blue shadings are upwelling and downwelling, respectively.

$$= \frac{\nabla \times \boldsymbol{\tau}}{\rho_0 (f+\zeta)} + \frac{\boldsymbol{\tau} \times \nabla\zeta}{\rho_0 (f+\zeta)^2}, \tag{3}$$

$$= \frac{\nabla \times \boldsymbol{\tau}}{\rho_0 (f+\zeta)} + \frac{1}{\rho_0 (f+\zeta)^2}\left(\tau_x \frac{\partial\zeta}{\partial y} - \tau_y \frac{\partial\zeta}{\partial x}\right), \tag{4}$$

where f is the Coriolis parameter and $\zeta = \partial v/\partial x - \partial u/\partial y$ is the geostrophic vorticity. According to equation (3), in the Southern Hemisphere where $f < 0$, a negative wind stress curl ($\nabla \times \tau$) and a positive $\tau \times \nabla\zeta$ result in a positive w_{tot}, that is, upwelling.

The vertical velocity driven by wind stress curl is increased through current-wind interaction. The annual mean w_{curl} averaged over the model domain in REL is close to 0.01 m day^{-1} while it is only 0.001 m day^{-1} in ABS (Figure 4a). Monthly average w_{curl} values are always greater in REL than ABS, suggesting that there is a net upward motion induced by the interaction between the current and wind. On the other hand, the net effect of the current-wind interaction on w_ζ is downwelling (Figure 4b). It moves the curve downward, and the positive annual mean w_ζ in ABS becomes negative in REL. Interestingly, the net effect of current-wind interaction on w_ζ is comparable to that in w_{curl} but in the opposite direction. As a result, the change in total Ekman velocity is close to zero (not shown).

The changes in w_{curl} and w_ζ induced by current-wind interaction arise in different ways which can be understood by considering the idealized meander (Figure 5) in which the flow is fastest at the core. The wind stress decreases near the core of the meander where the strength of the wind relative to the ocean current is at its minimum (Figure 5a). As a result, the wind stress curl is negative to the north of the core and positive to the south. The resulting vertical velocities in the Southern Hemisphere ($f < 0$) are upward and downward to the north and south of the core, respectively. The strength of these vertical velocities is further modified by the absolute vorticity ($f + \zeta$) according to (4) because the shear of the flow in the meander creates nonzero ζ. To the north of the core, $\zeta > 0$ and the upwelling becomes stronger. To the south of the core, in contrast, negative ζ increases the size of the absolute vorticity and weakens the downward motion. Since the size of ζ is smaller than f (Ro $\sim$ O(0.1)), $f + \zeta$ in the denominator has the same sign as f and so the sign of the curl-induced vertical velocity is not changed. Therefore, the net vertical motion is upward in w_{curl} when the current-wind interaction is included, thus accounting for Figure 4a.

When $\nabla\zeta$ is non-negligible, the horizontal shear of the flow can drive vertical motion (w_ζ) even in the absence of a wind stress curl. In both Northern and Southern Hemispheres, the upward motion occurs along with the core of the meander while the periphery is characterized by the downward motion as shown in Wenegrat and Thomas (2017) and sketched in Figure 5b. As above, w_ζ is modified by the absolute vorticity which has the opposite sign on each side of the core. Since w_ζ is inversely proportional to the square of the absolute vorticity, the impact of ζ is greater on w_ζ than on w_{curl}. But the systematic changes of w_ζ arise from the fact that the wind stress is at a minimum at the core of the meander. As explained above, the wind stress is weakest at the core of the jet where $w_\zeta > 0$, and so one can expect weakened upwelling following (4).

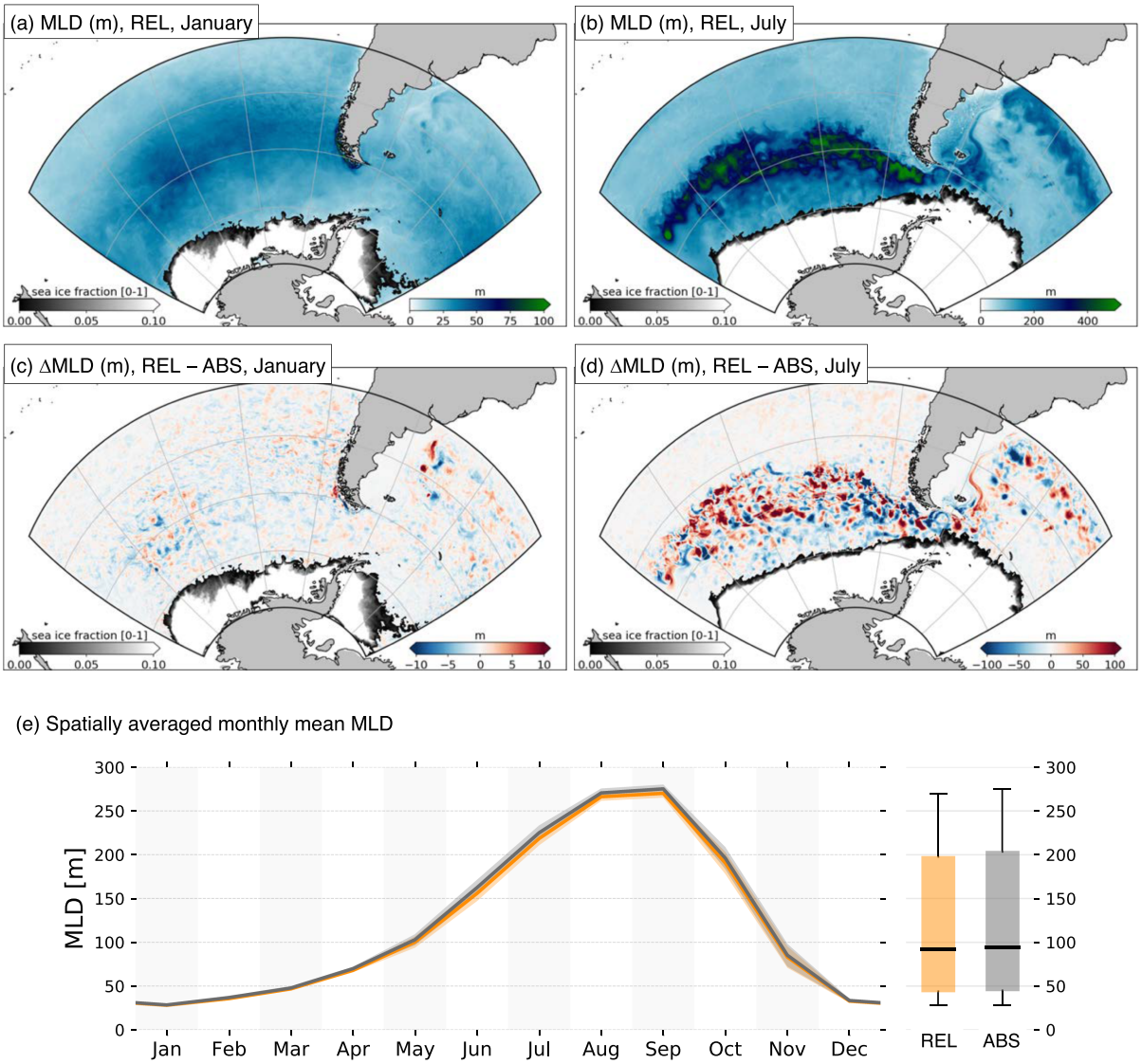

Figure 6. Monthly averaged mixed layer depth (MLD) in REL for (a) January and (b) July. The MLD differences between REL and ABS for those months are shown in (c) and (d), respectively. Panel (e) shows the monthly mean MLD along the ACC in REL (orange) and ABS (gray). The description of the bar plots is in Figure 1.

Although the downward motion in REL is also weakened relative to ABS due to overall reduced wind stress, $(u_a - u_o)$ is smaller than that at the core, resulting in a net negative w_ζ.

Scale analysis allows us to estimate expected wind-driven velocity changes. Using (1), the size of the wind stress curl can be related to the spatial changes in the current. For example, in the idealized meander system depicted in Figure 5 with $\tau_y = 0$ and at the crest or trough where $v_o = 0$, the scale of the wind stress curl is

$$\left|\frac{\partial \tau_x}{\partial y}\right| \sim \rho_a C_D \frac{2u_a U_o}{L}, \tag{5}$$

where u_a is the zonal wind, L is the spatial scale associated with the meander, and U_o measures the strength of the ocean current. The numerator of the second term in (4) can be written as

$$\left|\tau_x \frac{\partial \zeta}{\partial y}\right| \sim \rho_a C_D (u_a - u_o)^2 \frac{U_o}{L^2}. \tag{6}$$

Then, comparing the scales of the first and the second terms in (4), one can see that

$$\left|\frac{w_{curl}}{w_\zeta}\right| = 2u_a \frac{(f + \zeta)L}{(u_a - u_o)^2}. \tag{7}$$

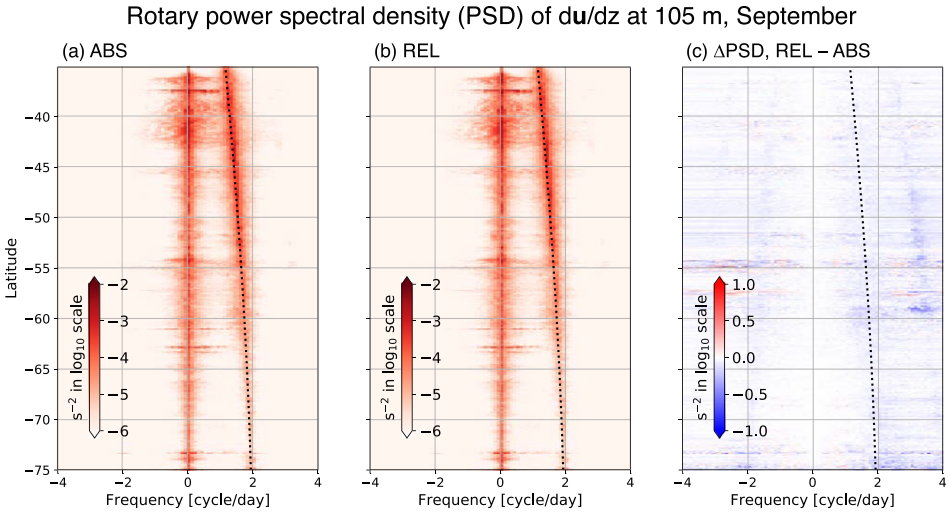

Figure 7. Rotary power spectral density of the ocean current vertical shear at 105 m in September as a function of frequency and latitude for (a) ABS and (b) REL. The rotary power spectral analysis reveals motions rotating in both counterclockwise (positive frequencies) and clockwise (negative frequencies). Panel (c) is the difference between (a) and (b). The color represents the intensity. The dotted lines indicate the inertial frequency at each latitude.

If we assume that $(u_a - u_o) \sim u_a$, and $(f + \zeta) \sim f$, (7) approaches 1 for $f = 10^{-4}$ s^{-1}, $L = 50$ km and $u_a = 10$ m s^{-1}, indicating that the changes in w_{curl} and w_ζ are similar.

The real Southern Ocean differs from our idealized system since asymmetric crests and troughs and well-developed eddies populate the ACC. Furthermore, the surface wind is not constant in time and space, adding yet more complexity. Sea surface temperature also varies spatially, especially near fronts, eddies, and meanders, affecting the wind in the planetary boundary layer through the changes in the vertical turbulent mixing (Byrne et al., 2015, 2016; Chelton et al., 2004; Seo et al., 2007), increasing the complexity of the real system. Nevertheless, the changes in w_{curl} and w_ζ observed in Figure 4 are consistent with the insights obtained from consideration of our idealized meander.

4.2. Vertical Mixing

The impact of current-wind interaction on near-surface vertical mixing is also of interest. Observations reveal large seasonality in the MLD, ranging from less than 100 m in austral summer to more than 500 m in austral winter in the study area (Dong et al., 2008). Our simulations, both ABS and REL, capture the large seasonal and spatial variability exhibited by MLD, as well as its modulation by mesoscale eddies (see Hausmann et al., 2017). For example, summertime MLD in REL is generally shallower than 50 m except to the north of the ACC where the MLD reaches 70 m or so (Figure 6a). In winter, the MLD is generally deeper near the northern boundary of the ACC, particularly in the Pacific sector, exceeding 500 m in REL (Figure 6b), which is consistent with observations.

The impact of the current-wind interaction on the local MLD can exceed 100 m, but it does not induce a coherent large-scale pattern of change in MLD. Differences are shown in Figures 6c and 6d and exhibit both positive and negative values on spatial scales similar to the mesoscale, O(10–100 km). Although the patchiness in the differences may be due to the relatively short integration of the model, it suggests that MLD changes are mainly due to the shift of the meander and eddy locations in both seasons. For example, the MLD anomalies associated with mesoscale eddies in this region average a few tens of meters in winter (Hausmann et al., 2017; Song et al., 2015). If REL and ABS have mesoscale eddies with opposite polarity at the same location, MLD differences between them can easily exceed 100 m (Figure 6d). In summer, observed MLD anomalies associated with mesoscale eddies are less than 10 m (Hausmann et al., 2017), comparable to the MLD differences between the two simulations (Figure 6c). These positive and negative MLD anomalies are generally canceled out in the spatial average so that the monthly mean MLD curves are very similar between the two simulations. A careful examination, however, reveals that MLD in REL is a few meters shallower than ABS (Figure 6e).

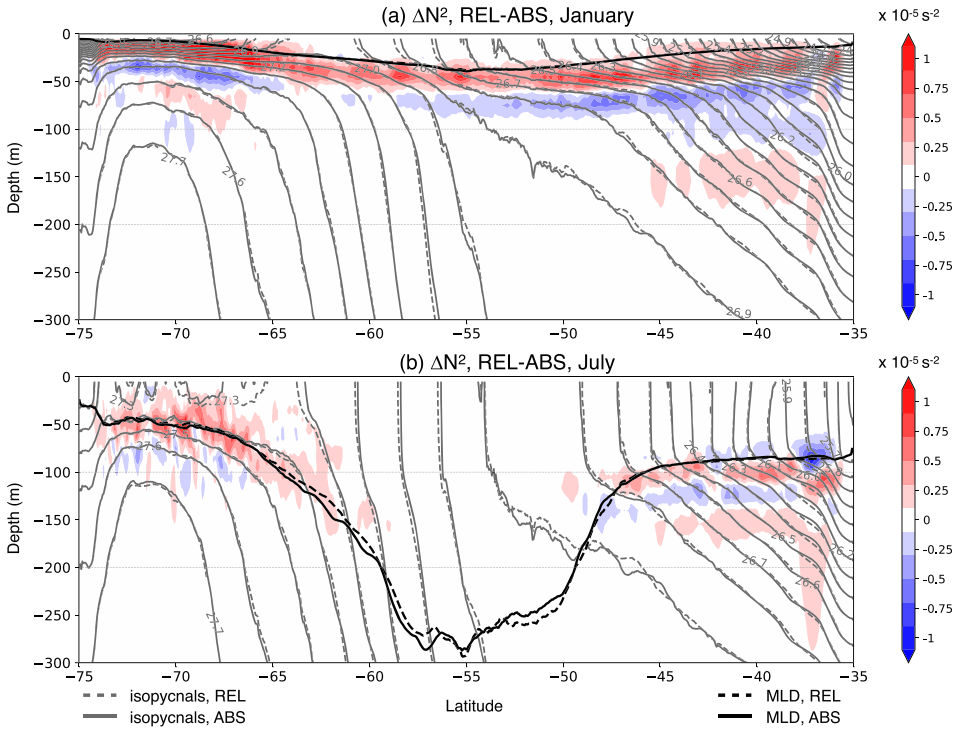

Figure 8. Shading represents the difference in the zonally averaged (from 155°*W* to 60°*W*) monthly mean Brunt-Vaisälä frequency (N^2) between REL and ABS (N^2_{REL} - N^2_{ABS}) in (a) January and (b) July. The black solid/dashed lines indicate the mean MLD in ABS and REL. The ΔN^2 and the MLDs in the boxes in (a) and (b) are zoomed in on the inset plots in each panel.

The KPP vertical mixing scheme used in our simulations determines the mixing depth based on a Richardson number defined by the ratio between the Brunt-Vaisälä frequency (N^2) and the vertical shear of the flow. Thus, small differences in MLD suggest that the Richardson numbers are rather similar in ABS and REL. To quantify, we first compute the rotary power spectral density of the vertical shear of the ocean currents at 105 m in both the ABS and REL runs in September (Figure 7). Two frequency bands show elevated power in both ABS and REL: one near zero associated with the geostrophic component and the other near the inertial frequency (f) in the positive frequency domain (Figures 7a and 7b). The elevated power near the frequency of the local f (dotted line in Figure 7) indicates that both simulations capture the near-inertial waves that are important in vertical mixing. In the Southern Hemisphere, near-inertial waves drive counterclockwise rotation with near-inertial frequency creating vertical shear and enhancing vertical mixing (Alford et al., 2016). Hence, the ability to resolve near-inertial waves has a big impact on MLD in our numerical simulations (Jochum et al., 2013; Song et al., 2019). A careful examination shows slightly less power in REL (on average less than 0.4% level in log space, Figure 7c), mainly in the frequency band higher than inertial due to the dampened eddy activities. However, both simulations clearly resolve near-inertial waves, indicating that the current-wind interaction does not significantly alter the generation of near-inertial waves. Although stratification changes are not significant within the mixed layer, there is a systematic increase of N^2 at the base of the mixed layer, as described below.

4.3. Stratification

Current-wind interaction causes change in the upper ocean stratification with increased N^2 at the bottom of the mixed layer (Figure 8). This pattern is more pronounced in the summer, when N^2 in REL is roughly 10% higher than N^2 in ABS (Figure 8a). In this season, N^2 is lower in REL than in ABS near the bottom of thermocline. It is plausible that there is an upward displacement of the thermocline in REL creating this dipole pattern in the N^2 difference, although the dipole pattern is not always present. We argue that this increase of N^2 is likely a result of weakening of wind-driven Ekman transport. Ekman transport is weaker in REL because the wind stress is weaker (Figure 1). As a result, the outcropping positions of the isopycnals in REL are further south than those in ABS. At the depth where the direct impact of the wind stress becomes

small, isopycnals in REL and ABS converge. Hence, the slopes of isopycnals in REL are more gradual than in ABS when connecting the isopycnals at the surface to depth.

One might anticipate a decrease in MLD in REL based on the enhanced stratification, especially in austral summer. Although a closer inspection indicates that the MLD (black thick lines in Figure 8) is slightly shallower in REL, it generally remains unchanged as the increase of N^2 occurs largely below the mixed layer.

In winter when vertical mixing homogenizes the surface layer, the background N^2 is already small, and isopycnals are almost vertical near the surface. Although the isopycnals are shifted poleward near the surface in REL due to the weaker wind stress, the interaction between the current and wind does not alter stratification as much as in summer, perhaps because of the absence of a well-developed thermocline. This is particularly true near the ACC, showing no changes in N^2 (Figure 8b). However, the tendency for an N^2 increase near the bottom of the mixed layer remains, suggesting that the current-wind interaction tends to increase the stratification at the base of the mixed layer.

5. Discussion and Conclusion

Ocean currents are often neglected in the calculation of wind stress because typically surface current speeds are one order of magnitude smaller than the 10-m wind. However, previous studies have shown that the presence of ocean currents can have a non-negligible effect on wind stress and the ocean's EKE. In the Southern Ocean, numerical studies with idealized models report that current-wind interaction reduces the EKE by up to 18% (Hutchinson et al., 2010; Munday & Zhai, 2015). Indeed, satellite observations suggest that the impact of current-wind interaction is especially large in the Southern Ocean (Renault, McWilliams, & Masson, 2017). Here, we have extended the investigation of current-wind interaction to explore its impact on vertical processes such as wind-driven vertical velocity and vertical mixing using a 0.05° resolution ocean-only model encompassing the Drake passage.

Our experiment shows a 24% reduction in surface EKE using the relative wind stress. As a result, the EKE bias in the simulations with absolute wind is alleviated. The size of the EKE reduction is somewhat larger than reported in previous idealized studies, possibly due to the increased resolution employed here. The EKE reduction is not limited to the surface but extends to depths of 1,000 m or more where EKE is reduced by 13%. The effect also persists throughout the year. A comparison of major contributors to energy conversion shows that the reduced EKE is a consequence of a weaker wind work.

The wind-induced vertical velocity is also modified by the interaction. By consideration of an idealized meandering jet system in the Southern Hemisphere ($f < 0$), one can anticipate that positive relative vorticity in a meander crest will amplify upward motion, while negative relative vorticity in a meander trough will weaken downward motion. The overall contribution from the wind stress curl created by the current-wind interaction is therefore one of upwelling. On the other hand, nonlinear contributions to the wind-driven vertical velocity (w_ζ) induce a net downward motion due to the interaction. Near the core of the jet where $\nabla\zeta$ is positive, upwelling occurs which contrasts with downwelling outside of the jet. If the ocean current is taken into account in the wind stress calculation, the wind stress over the core of the jet becomes weaker than outside, leading to a net negative change in w_ζ. Interestingly, the changes in w_{curl} and w_ζ compensate each other, such that the net changes in the wind-driven vertical velocity are rather small in our simulation.

One may anticipate a shoaling of the MLD in REL since both the momentum transfer from the atmosphere and EKE are reduced. In our experiment, however, the MLD shows only modest changes in the spatial mean. The magnitude of MLD anomalies are considerable in some locations, but this is the result of the shift of locations of meanders and eddies. Further analysis shows that there are no significant changes in the vertical shear of the flow and stratification within the mixed layer, leading to little change in the Richardson number. Interestingly, the rotary power spectral density functions of du/dz show little difference between ABS and REL, which suggests that the near-inertial waves have similar amplitude in both cases and hence there is no modulation of shear-induced mixing. In the K-profile parameterization used in our simulations, the mixing depth is determined by the Richardson number, which may explain why there are rather small net MLD changes caused by current-wind interaction. It is possible that vertical mixing schemes based on turbulent kinetic energy budgets may induce a shoaling of the MLD.

Another factor that may lead to insensitivity of the MLD is the influence of the upstream open boundary condition. In our study area, the eastward flow constantly enters from the western boundary (160°W), feeding the same water mass to the interior of ABS and REL. This eastward flow includes the ACC that can be up to 50 cm s^{-1}. It then takes roughly only 180 days to exit downstream (20°W). Hence, even if the current-wind interaction was to modify the MLD, inflow from the upstream boundary continuously resets the water properties in ABS and REL to the values at the western boundary condition, possibly leading to smaller MLD changes.

Below the mixed layer there is a clear increase in stratification due to current-wind interaction. In summer, there is a roughly 10% increase of the Brunt-Vaisälä frequency (N^2) in REL over a few tens of meters. Although this tendency is attenuated in winter, it remains in the thermocline. The current-wind interaction reduces overall eastward wind stress to the ocean, leading to a weaker equatorward Ekman transport. Isopycnals thus outcrop further south in REL while their latitudinal position below the Ekman layer is barely changed. As a result, the slopes of isopycnals in REL are more gradual than those in ABS, yielding enhanced stratification below the mixed layer.

This result may appear to contradict the conclusion of Munday and Zhai (2015) in which the isopycnals become steeper when the wind stress is calculated using both 10-m wind and ocean current (relative wind stress) in an idealized channel model. This statement is can be applied when comparing this simulation with the one where the wind stress is calculated using a 10-m wind adjusted to have the same mean value as the relative wind stress simulation so that the Ekman transport is unchanged. A closer observation of Figure 5 in Munday and Zhai (2015), however, reveals that the relative wind stress simulation has isopycnal outcrops further south than the resting ocean run (absolute wind stress) near the position of the zonal wind maximum, which is consistent with our results.

Future work will address the biogeochemical implications of our findings, as biological and chemical processes can be sensitive to subtle changes in ocean physics due to their intrinsic nonlinearity. Specifically, changes in stratification and upwelling rates can modulate biogeochemical processes in the Southern Ocean due to lack of iron and light available for the primary production (Boyd et al., 1999, 2000; Venables & Moore, 2010). In addition to supply of iron through dust deposition, sediment, and sea ice melt, vertical mixing is an important process since it entrains iron-rich subsurface waters (Boyd & Ellwood, 2010; Tagliabue et al., 2014). In summer when light is abundant, satellite observations and eddy-rich biogeochemical simulations show a positive correlation between anomalies of sea level and chlorophyll, suggesting that anomalously deep vertical mixing increases the iron supply and primary production (Song et al., 2018). Hence, increased stratification in the thermocline induced by current-wind interaction may make entrainment of iron-rich water more sporadic thus suppressing primary productivity.

Current-wind interaction can also influence air-sea carbon dioxide (CO_2) exchange. Dissolved inorganic carbon (DIC), whose concentration increases poleward in the Southern Ocean, may have lower surface concentrations under weaker Ekman transport with the relative wind stress in both summer and winter. This could cause reduction in the partial pressure of CO_2 (pCO_2), leading to more CO_2 uptake in summer and less outgassing in winter. On the other hand, there may be a decrease in the biological drawdown of CO_2 in summer as discussed above, which would counterbalance the changes in the Ekman transport. Hence, it is necessary to thoroughly investigate the impact of the current-wind interaction on the carbon cycle in the Southern Ocean.

Acknowledgments
The MITgcm can be obtained online (http://mitgcm.org). The geostrophic current product derived from the sea level anomaly can be downloaded in the Copernicus Marine and Environment Monitoring Service of Ssalto/Duacs gridded "allsat" series and along-track Sea Level Anomalies, Absolute Dynamic Topographies and Geostrophic velocities over the Global Ocean, Mediterranean Sea, Black Sea, European Seas and Acrtic Ocean areas, in Delayed-Time and in Near-Real-Time. Resources supporting this work were provided by the NASA High-End Computing (HEC) Program through the NASA Advanced Supercomputing (NAS) Division at Ames Research Center with the award number SMD-15-5752. H. S., J. M., and D. J. M. were supported by the NSF MOBY project (OCE-1048926 and OCE-1048897). H. S. acknowledges the support by National Research Foundation of Korea (NRF) grant funded by the Korea government (MSIT) (NRF-2019R1C1C1003663) and Yonsei University Research Fund of 2018-22-0053. D. J. M. also gratefully acknowledges NSF and NASA support, along with the Holger W. Jannasch and Columbus O'Donnell Iselin shared chairs for Excellence in Oceanography. H. Seo acknowledges the support from the ONR (N00014-17-1-2398), NOAA (NA10OAR4310376), and the Andrew W. Mellon Foundation Endowed Fund for Innovative Research at WHOI. We also thank two anonymous referees whose comments significantly improved the presentation of results.

References

Adcroft, A., Hill, C., Campin, J.-M., Marshall, J., & Heimbach, P. (2004). Overview of the formulation and numerics of the MIT GCM. In *Proceedings of the ECMWF Seminar Series on Numerical Methods, Recent Developments in Numerical Methods for Atmosphere and Ocean Modelling* (pp. 139–149). ECMWF.

Adcroft, A. J., Hill, C. N., & Marshall, J. (1997). Representation of topography by shaved cells in a height coordinate ocean model. *Monthly Weather Review*, *125*, 2293–2315.

Alford, M. H., MacKinnon, J. A., Simmons, H. L., & Nash, J. D. (2016). Near-inertial internal gravity waves in the ocean. *Annual Review of Marine Science*, *8*(1), 95–123. https://doi.org/10.1146/annurev-marine-010814-015746

Boyd, P. W., & Ellwood, M. J. (2010). The biogeochemical cycle of iron in the ocean. *Nature Geoscience*, *3*, 675–682.

Boyd, P. W., LaRoche, J., Gall, M., Frew, R., & McKay, R. M. L. (1999). Role of iron, light, and silicate in controlling algal biomass in subantarctic waters S. E. of New Zealand. *Journal of Geophysical Research*, *104*(C6), 13,395–13,408. https://doi.org/10.1029/1999JC900009

Boyd, P. W., Watson, A. J., Law, C. S., Abraham, E. R., Trull, T., Murdoch, R., et al. (2000). A mesoscale phytoplankton bloom in the polar Southern Ocean stimulated by iron fertilization. *Nature*, *407*(6805), 695–702.

Byrne, D., Münnich, M., Frenger, I., & Gruber, N. (2016). Mesoscale atmosphere ocean coupling enhances the transfer of wind energy into the ocean. *Nature Communications*, *7*, ncomms11867. https://doi.org/10.1038/ncomms11867

Byrne, D., Papritz, L., Frenger, I., Münnich, M., & Gruber, N. (2015). Atmospheric response to mesoscale sea surface temperature anomalies: Assessment of mechanisms and coupling strength in a high-resolution coupled model over the South Atlantic. *Journal of the Atmospheric Sciences*, *72*, 1872–1890. https://doi.org/10.1175/JAS-D-14-0195.1

Chelton, D. B., DeSzoeke, R., Schlax, M., El Naggar, K., & Siwertz, N. (1998). Geographical variability of the first baroclinic Rossby radius of deformation. *Journal of Physical Oceanography*, *28*, 433–460.

Chelton, D. B., Schlax, M. G., Freilich, M. H., & Milliff, R. F. (2004). Satellite measurements reveal persistent small-scale features in ocean winds. *Science*, *303*(5660), 978–983.

Dawe, J. T., & Thompson, L. (2006). Effect of ocean surface currents on wind stress, heat flux, and wind power input to the ocean. *Geophysical Research Letters*, *33*, L09604. https://doi.org/10.1029/2006GL025784

de Boyer Montégut, C., Madec, G., Fischer, A. S., Lazar, A., & Iudicone, D. (2004). Mixed layer depth over the global ocean: An examination of profile data and a profile-based climatology. *Journal of Geophysical Research*, *109*, C12003. https://doi.org/10.1029/2004JC002378

Dewar, W. K., & Flierl, G. R. (1987). Some effects of the wind on rings. *Journal of Physical Oceanography*, *17*, 1653–1667.

Dohan, K., & Maximenko, N. (2010). Monitoring ocean currents with satellite sensors. *Oceanography*, *23*(4), 94–103. https://doi.org/10.5670/oceanog.2010.08

Dong, S., Sprintall, J., Gille, S. T., & Talley, L. (2008). Southern Ocean mixed-layer depth from Argo float profiles. *Journal of Geophysical Research*, *113*, C06013. https://doi.org/10.1029/2006JC004051

Duhaut, T. H. A., & Straub, D. N. (2006). Wind stress dependence on ocean surface velocity: Implications for mechanical energy input to ocean circulation. *Journal of Physical Oceanography*, *36*, 202–211. https://doi.org/10.1175/JPO2842.1

Eden, C., & Dietze, H. (2009). Effects of mesoscale eddy/wind interactions on biological new production and eddy kinetic energy. *Journal of Geophysical Research*, *114*, C05023. https://doi.org/10.1029/2008JC005129

Forget, G. (2010). Mapping ocean observations in a dynamical framework: A 2004-06 ocean atlas. *Journal of Physical Oceanography*, *40*(6), 1201–1221.

Hausmann, U., McGillicuddy, D. J., & Marshall, J. (2017). Observed mesoscale eddy signatures in Southern Ocean surface mixed-layer depth. *Journal of Geophysical Research: Oceans,122*, 617–635. https://doi.org/10.1002/2016JC012225

Holte, J., & Talley, L. (2009). A new algorithm for finding mixed layer depths with applications to Argo data and subantarctic mode water formation. *Journal of Atmospheric and Oceanic Technology*, *26*(9), 1920–1939.

Hutchinson, D. K., Hogg, A. M. C., Blundell, J. R., Hutchinson, D. K., Hogg, A. M. C., & Blundell, J. R. (2010). Southern Ocean response to relative velocity wind stress forcing. *Journal of Physical Oceanography*, *40*(2), 326–339.

Jochum, M., Briegleb, B. P., Danabasoglu, G., Large, W. G., Norton, N. J., Jayne, S. R., et al. (2013). The impact of oceanic near-inertial waves on climate. *Journal Climate*, *26*, 2833–2844.

Large, W. G., McWilliams, J., & Doney, S. (1994). Oceanic vertical mixing: A review and a model with nonlocal boundary layer parameterization. *Reviews of Geophysics*, *32*(4), 363–403.

Large, W. G., & Yeager, S. G. (2004). Diurnal to decadal global forcing for ocean and sea-ice models: The data sets and flux climatologies. Ncar technical note: Ncar/tn-460+str, CGD Division of National Center for Atmospheric Research Boulder.

Laurindo, L. C., Mariano, A. J., & Lumpkin, R. (2017). An improved near-surface velocity climatology for the global ocean from drifter observations. *Deep-Sea Research Part I*, *124*, 73–92. https://doi.org/10.1016/j.dsr.2017.04.009

Marchesiello, P., McWilliams, J. C., & Shchepetkin, A. (2003). Equilibrium structure and dynamics of the California Current System. *Journal of Physical Oceanography*, *33*, 753–783. https://doi.org/10.1175/1520-0485(2003)33,753:ESADOT.2.0.CO;2

Marshall, J., Adcroft, A., Hill, C., Perelman, L., & Heisey, C. (1997). A finite-volume, incompressible Navier Stokes model for studies of the ocean on parallel computers. *Journal of Geophysical Research*, *102*(C3), 5753–5766.

Marshall, J., Hill, C., Perelman, L., & Adcroft, A. (1997). Hydrostatic, quasi-hydrostatic, and nonhydrostatic ocean modeling. *Journal of Geophysical Research*, *102*(C3), 5733–5752.

Marshall, J., Jones, H., & Hill, C. (1998). Efficient ocean modeling using non-hydrostatic algorithms. *Journal of Marine Systems*, *18*, 115–134.

Maximenko, N. A., Niiler, P. P., Rio, M., Melnichenko, O., Centurioni, L., Chambers, D., et al. (2009). Mean dynamic topography of the ocean derived from satellite and drifting buoy data using three different techniques. *Journal of Atmospheric and Oceanic Technology*, *26*, 1910–1918.

McGillicuddy, D. J., Ledwell, J., & Anderson, L. (2008). Response to comments on "eddy/wind interactions stimulate extraordinary mid-ocean plankton blooms". *Sciences*, *320*, 488. https://doi.org/10.1126/science.1148974

Munday, D. R., & Zhai, X. (2015). Sensitivity of Southern Ocean circulation to wind stress changes: Role of relative wind stress. *Ocean Modelling*, *95*, 15–24.

Niiler, P. P. (1969). On the Ekman divergence in an oceanic jet. *Journal of Geophysical Research*, *74*, 7048–7052. https://doi.org/10.1029/JC074i028p07048

Oerder, V., Colas, F., Echevin, V., Masson, S., & Lemarié, F (2018). Impacts of the mesoscale ocean-atmosphere coupling on the Peru-Chile ocean dynamics: The current-induced wind stress modulation. *Journal of Geophysical Research: Oceans*, *123*, 812–833. https://doi.org/10.1002/2017JC013294

Renault, L., McWilliams, J. C., & Masson, S. (2017). Satellite observations of imprint of oceanic current on wind stress by air-sea coupling. *Scientific Reports*, *7*(1), 17,747.

Renault, L., McWilliams, J. C., & Penven, P. (2017). Modulation of the Agulhas Current retroflection and leakage by oceanic current interaction with the atmosphere in coupled simulations. *Journal of Physical Oceanography*, *47*(8), 2077–2100.

Renault, L., Molemaker, M. J., Gula, J., Masson, S., & McWilliams, J. C. (2016). Control and stabilization of the Gulf Stream by oceanic current interaction with the atmosphere. *Journal of Physical Oceanography*, *46*, 3439–3453.

Renault, L., Molemaker, M. J., McWilliams, J. C., Shchepetkin, A. F., Lemarié, F., Chelton, D., et al. (2016). Modulation of wind work by oceanic current interaction with the atmosphere. *Journal of Physical Oceanography*, *46*, 1685–1704.

Seo, H. (2017). Distinct influence of air-sea interactions mediated by mesoscale sea surface temperature and surface current in the Arabian Sea. *Journal Climate*, *30*(20), 8061–8080.

Seo, H., Jochum, M., Murtugudde, R., Miller, A. J., & Roads, J. O. (2007). Feedback of tropical instability-wave-induced atmospheric variability onto the ocean. *Journal Climate*, *20*(23), 5842–5855.

Seo, H., Miller, A. J., & Norris, J. R. (2016). Eddy-wind interaction in the California Current System: Dynamics and impacts. *Journal of Physical Oceanography*, *46*(2), 439–459. https://doi.org/10.1175/JPO-D-15-0086.1

Seo, H., Subramanian, A. C., Song, H., & Chowdary, J. S. (2019). Coupled effects of ocean current on wind stress in the Bay of Bengal: Eddy energetics and upper ocean stratification. *Deep-Sea Research II*, *168*, 104617. https://doi.org/10.1016/j.dsr2.2019.07.005

Simmons, A., Uppala, S., Dee, D., & Kobayashi, S. (2007). ERA-Interim: New ECMWF reanalysis products from 1989 onwards. *ECMWF Newsletter*, 110, 1–11.

Song, H., Long, M. C., Gaube, P., Frenger, I., Marshall, J., & McGillicuddy, D. J. (2018). Seasonal variation in the correlation between anomalies of sea level and chlorophyll in the Antarctic circumpolar current. *Geophysical Research Letters*, *45*, 5011–5019. https://doi.org/10.1029/2017GL076246

Song, H., Marshall, J., Campin, J.-M., & McGillicuddy, D. J. (2019). Impact of near-inertial waves on vertical mixing and air-sea CO_2 fluxes in the Southern Ocean. *Journal of Geophysical Research: Oceans*, *124*, 4605–4617. https://doi.org/10.1029/2018JC014928

Song, H., Marshall, J., Gaube, P., & McGillicuddy, D. J. (2015). Anomalous chlorofluorocarbon uptake by mesoscale eddies in the Drake Passage region. *Journal of Geophysical Research: Oceans*, *120*, 1065–1078. https://doi.org/10.1002/2014JC010292

Song, H., Marshall, J., Munro, D. R., Dutkiewicz, S., Sweeney, C., McGillicuddy, D. J., & Hausmann, U. (2016). Mesoscale modulation of air-sea CO_2 flux in Drake Passage. *Journal of Geophysical Research: Oceans*, *121*, 6635–6649. https://doi.org/10.1002/2016JC011714

Stern, M. (1965). Interaction of a uniform wind stress with a geostrophic vortex. *Deep Sea Research and Oceanographic Abstracts*, *12*, 355–367. https://doi.org/10.1016/0011-7471(65)90007-0

Tagliabue, A., Sallée, J.-B., Bowie, A. R., Lévy, M., Swart, S., & Boyd, P. W. (2014). Surface-water iron supplies in the Southern Ocean sustained by deep winter mixing. *Nature Geoscience*, *7*, 314–320. https://doi.org/10.1038/ngeo2101

Talley, L. D., Pickard, G. L., Emery, W. J., & Swift, J. H. (2011). *Descriptive physical oceanography: An introduction* (6th ed.). Oxford: Academic Press.

Tsujino, H., Urakawa, S., Nakano, H., Small, R. J., Kim, W. M., Yeager, S. G., et al. (2018). JRA-55 based surface dataset for driving ocean-sea-ice models (JRA55-do). *Ocean Modelling*, *130*, 79–139. https://doi.org/10.1016/j.ocemod.2018.07.002

Tulloch, R., Ferrari, R., Jahn, O., Klocker, A., LaCasce, J., Ledwell, J., et al. (2014). Direct estimates of lateral eddy diffusivity upstream of Drake Passage. *Journal of Physical Oceanography*, *44*, 2593–2616.

Tulloch, R., Marshall, J., Hill, C., & Smith, K. S. (2011). Scales, growth rates, and spectral fluxes of baroclinic instability in the ocean. *Journal of Physical Oceanography*, *41*(6), 1057–1076. https://doi.org/10.1175/2011JPO4404.1

Venables, H., & Moore, C. M. (2010). Phytoplankton and light limitation in the Southern Ocean: Learning from high-nutrient, high-chlorophyll areas. *Journal of Geophysical Research*, *115*, C02015. https://doi.org/10.1029/2009JC005361

Wenegrat, J. O., & Thomas, L. N. (2017). Ekman transport in balanced currents with curvature. *Journal of Physical Oceanography*, *47*, 1189–1203. https://doi.org/10.1175/JPO-D-16-0239.1

Wunsch, C. (2007). The past and future ocean circulation from a contemporary perspective. In A. Schmittner, J. C. Chiang, & S. R. Hemming (Eds.), *Ocean circulation: Mechanisms and impacts–past and future changes of meridional overturning* (pp. 53–74). Washington DC: American Geophysical Union. https://doi.org/10.1029/173GM06

Zhai, X., & Greatbatch, R. J. (2007). Wind work in a model of the northwest Atlantic Ocean. *Geophysical Research Letters*, *34*, L04606. https://doi.org/10.1029/2006GL028907

Zhai, X., Johnson, H. L., Marshall, D. P., & Wunsch, C. (2012). On the wind power input to the ocean general circulation. *Journal of Physical Oceanography*, *42*(8), 1357–1365.

Zhan, P., Subramanian, A. C., Yao, F., Kartadikaria, A. R., Guo, D., & Hoteit, I. (2016). The eddy kinetic energy budget in the Red Sea. *Journal of Geophysical Research: Oceans*, *121*, 4732–4747. https://doi.org/10.1002/2015JC011589